The first X-ray spectrum of the high-mass X-ray binary XTE J1855−026 during the compact object eclipse

G. Sanjurjo-Ferrín,★ J. M. Torrejón ⬛ and J. J. Rodes-Roca

Instituto Universitario de Física Aplicada a las Ciencias y las Tecnologías, Universidad de Alicante, E-03690 Alicante, Spain

ABSTRACT

We present the first *XMM–Newton* observation of the classical supergiant high-mass X-ray binary XTE J1855−026 taken entirely during the eclipse of the neutron star (NS), covering the orbital phases $\phi = 0.00$–0.11. The analysis of the data allows us to (a) compare with the parameters obtained during the existing pre-eclipse observation and (b) explore the back-illuminated stellar wind of the B0I-type donor. The blackbody component, used to describe the soft excess during pre-eclipse, is not observed during eclipse. It must be then produced near the NS or along the donor–NS line. The 0.3–10 keV luminosity during eclipse ($\sim 10^{34}$ erg s^{-1}) is 70 times lower than pre-eclipse. The intensity of the Fe Kα line, in the average eclipse spectrum, is ~ 7.4 times lower than the one measured during pre-eclipse. Since Kα photons cannot be resonantly scattered in the wind, the vast majority of Fe Kα emission must come from distances within $1R_*$ from the NS. The eclipse spectrum is successfully modelled through the addition of two photoionized plasmas, one with low ionization ($\log \xi_{1,\mathrm{cold}} = 0.36$) and high emission measure (EM$_{1,\mathrm{cold}}$ $\approx 3 \times 10^{59}$ cm^{-3}) and another with high ionization ($\log \xi_{2,\mathrm{hot}} = 3.7$) and low emission measure (EM$_{2,\mathrm{hot}} \approx 2 \times 10^{56}$ cm^{-3}). Assuming that the cold and hot gas phases are the clumps and the interclump medium of the stellar wind, respectively, and a clump volume filling factor of ≈ 0.04–0.05, typical for massive stars, a density contrast between clumps and the interclump medium of $n_c/n_i \approx 180$ is deduced, in agreement with theoretical expectations and optical–ultraviolet observations of massive star winds.

Key words: stars: massive – X-rays: binaries – X-rays: individual: XTE J1855−026.

1 INTRODUCTION

Supergiant X-ray binaries (SGXBs) are the high-mass X-ray binaries (HMXBs) where a compact object (a neutron star – NS – or a black hole) orbits an evolved massive star (the companion) in its supergiant phase, accreting matter from its powerful stellar wind. HMXBs have been a prime target since the dawn of X-ray astronomy (see Kretschmar et al. 2019, for a recent review). Interest in these systems has been revamped in the last years for two reasons. First, they are the natural progenitors of the double degenerate binaries whose coalescence produces the gravitational waves predicted by the general theory of relativity and now finally detected (Abbott et al. 2016; van den Heuvel 2019). To characterize the physical properties of the parent population is of paramount importance. Secondly, they are prime laboratories to study the stellar winds in massive stars (Martínez-Núñez et al. 2017). Massive stars ($M_i > 8 \, \mathrm{M}_\odot$) are among the main drivers of the evolution of star clusters and galaxies. Their powerful stellar winds and their final supernova explosions inject large amounts of matter and mechanical energy into their environments, thus enriching the interstellar medium (ISM) and further triggering star formation. Yet, the structure and properties of massive star winds are still poorly known.

The accretion of matter from the stellar wind on to an NS powers strong X-ray radiation, which, in turn, illuminates nearby wind regions. This radiation excites transitions in the stellar wind, producing emission lines of different elements. These line intensities change relative to continuum with the orbital phase, been specially enhanced during the eclipse, when the direct continuum produced by the NS is blocked by the optical counterpart (Torrejón et al. 2015; Aftab, Paul & Kretschmar 2019; Martínez-Chicharro et al. 2021). Thus, eclipsing systems with supergiant companions are particularly well suited to study the irradiated stellar wind. The stellar wind properties (v_∞, $\dot{M}$, $\rho(r)$) and the binary system characteristics (R_*, a) combine to influence the observed X-ray spectrum [most notably, through the ionization parameter $\xi = L_X/n(r_X)r_X^2$], and these change, among other things, with the donor's spectral type. A continuum of types would, thus, be desirable but, unfortunately, there are only a handful of such systems. Characterizing them all is, thus, very important.

The X-ray source, XTE J1855−026, was discovered by the *Rossi X-ray Timing Explorer* (*RXTE*) satellite (Corbet et al. 1999). The source contains an NS showing a $\simeq 361$ s X-ray pulse, orbiting the companion every ~ 6 d. Through the analysis of the eclipse duration, Corbet & Mukai (2002) suggest a massive companion with a radius corresponding to a B0I donor. This is further supported through the spectral energy distribution fitting (Coleiro & Chaty 2013), as well as through direct optical spectrum fitting, which refines the spectral type to B0Iaep (González-Galán 2016). The distance to XTE J1855−026, derived from the European Space Agency mission *Gaia*,[1] is 7.4 ± 0.8 kpc, using the combined parallax measure and

---

★ E-mail: graciela@sanal.es

[1] https://www.cosmos.esa.int/gaia

Table 1. Properties of XTE J1855−026 system.

	Companion	
MK type	B0Iaep	1, 2
M_{opt}	21 M$_\odot$	3
R_*	22 R$_\odot$	3
	Neutron star	
M_{NS}	1.4 M$_\odot$	1
Spin period	360.7 s	1
$\dot{P}/P$	$-12(13) \times 10^{-6}$ yr^{-1}	3
	System	
Orbital period	6.07415(8) d	3
i	71°(2°)	3
Eccentricity	0.04(2)	1
Orbital radius	1.8 R_*	Deduced
Orbital velocity	330 km s^{-1}	Deduced
Distance	7.4 ± 0.8 kpc	4
T_0 (MJD)	52 704.009(17)	3

Note. (1) Corbet & Mukai (2002), (2) González-Galán (2016), (3) Falanga et al. (2015), (4) Bailer-Jones et al. (2021), and (5) Bailer-Jones et al. (2021).
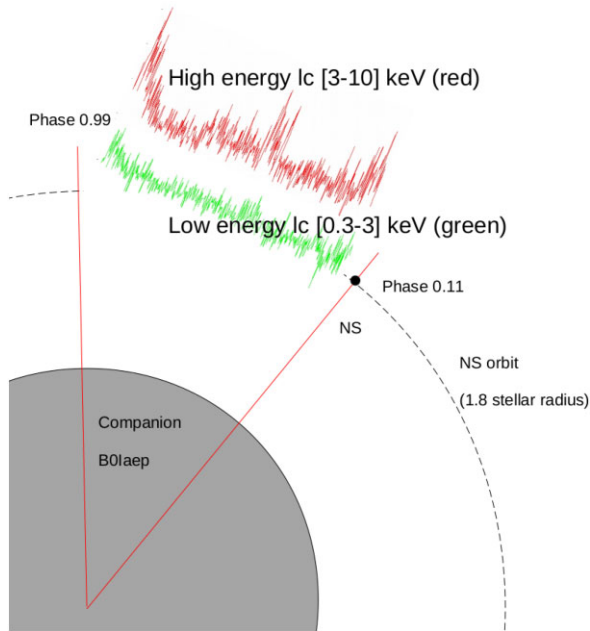

Figure 1. Pole-on sketch of the system and orbital phases covered by the *XMM–Newton* observation, using the ephemerides of Falanga et al. (2015). The donor star radius and the orbit are to scale.

the source's *G*-band magnitude and BP-RP colour (Bailer-Jones et al. 2021). In Table 1, we compile the system parameters relevant for this work. In Fig. 1, we show a sketch of the system where the orbit and the donor radius are to scale.

Devasia & Paul (2018) present the only low-resolution CCD X-ray spectral analysis using *Suzaku* data. This observation was performed entirely out of eclipse, just prior to ingress. In this paper, we present the analysis of the first observation of XTE J1855−026, taken entirely during eclipse, using the *X-ray Multi-Mirror Mission* (*XMM–Newton*) space observatory. These data are used to analyse the emission line spectrum with unprecedented detail.

Table 2. *XMM–Newton* observation log.

Observation ID	Date	Orbital phase	Duration (ks)
0844630101	2020/3/21	0.99–0.11	60

2 OBSERVATION AND ANALYSIS

The *XMM–Newton* spacecraft carries three high-throughput X-ray telescopes and one optical monitor. The European Photon Imaging Camera (EPIC) focal plane instruments, pn, MOS1, and MOS2, provide broad-band coverage ($E \sim 0.3$–10 keV) with a moderate spectral resolution ($E/\Delta E \sim 20$–50). The Reflection Grating Spectrometer provides high-resolution spectra ($E/\Delta E \sim 150$–800) over a limited spectral range $E \sim 0.3$–2.1 keV. In Table 2, we present the observation log.

The observation was carried out using medium filters for the three EPIC focal plane instruments MOS1, MOS2, and pn. The three cameras were operating in large window mode. The data were first processed through the pipeline chains and filtered. For MOS1 and MOS2, only events with a pattern between 0 and 12 were considered, filtered through #XMMEA EM. For pn, we kept events with `flag = 0` and a pattern between 0 and 4 (Turner et al. 2001). The chosen extraction region was a circle centred in the brightest point of the source. The background selected was an annulus around the extraction region. We checked whether the observations were affected by pile-up, using the `epatplot` task, with negative results.

The spectra were produced with a spectral bin size of 6 and analysed and modelled with the Interactive Spectral Interpretation System (ISIS) package (Houck 2002).[2] The data from the three cameras, MOS1, MOS2, and pn, were finally combined using the task `epicspeccombine` for the analysis. The energy range used for spectral fitting was 0.35–10 keV. The errors were obtained with the `fit_pars` and the `conf` tasks, provided by ISIS, for a 90 per cent confidence level. The emission lines were identified, thanks to the ATOMDB[3] data base and the *X-ray Data Booklet* (Thompson 2001).

The light-curve timing analysis was performed by combining the light curves from the three cameras (MOS1, MOS2, and pn) using the task `lcmath`. The photon arrival times were transformed to the Solar system barycentre.

The observation took place entirely during the eclipse of the X-ray source, as the 99 per cent of the X-ray flux is occulted between phases 0.92 and 0.097 (Falanga et al. 2015). Even when the last flare is out of this range, it is only by $\phi_{orb} = 1°.3$ and a return to a low number of counts is observed at the end of the section.

3 RESULTS

3.1 X-ray light curve

The light curve, produced by combining data from the three EPIC cameras, is shown in Fig. 2 for the 3–10 (red) and 0.2–3 keV (green) energy ranges. The colour ratio CR = (3–10)/(0.2–3) (black) is also plotted. In general, it looks stable. This is expected during the X-ray eclipse. However, some variability is still observed. Consequently, the light curve was further divided into six intervals: three plateaus
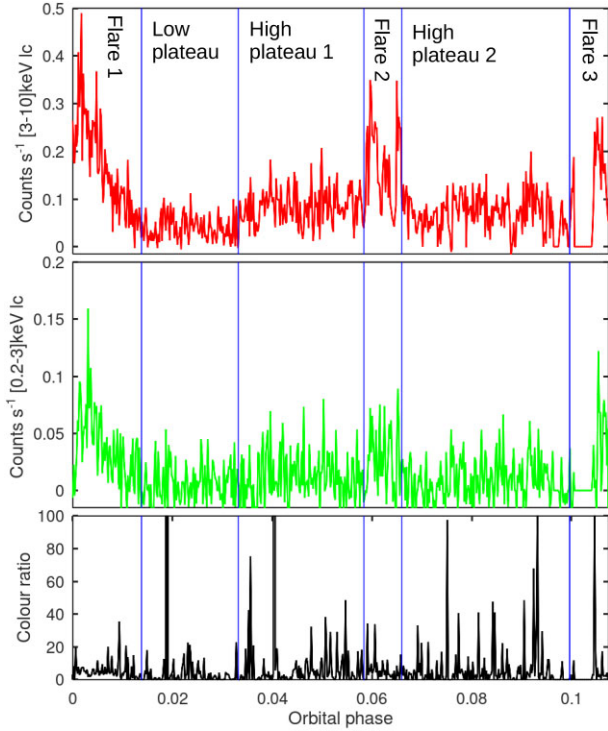
[2]maintained by MIT at https://space.mit.edu/cxc/isis/
[3]http://www.atomdb.org/

Figure 2. *XMM–Newton* EPIC light curves of XTE J1855−026 for the 3–10 keV (red, upper panel), 0.2–3 keV (green, middle panel) energy ranges along with the colour ratio CR = (3–10)/(0.2–3) (black, lower panel). The divisions show the six different sections into which the observation was divided, according to the source flux. The time bin is 150 s.

Table 3. Weighted average count rate per interval (Fig. 2).

	Weighted mean (counts s^{-1}) $\times 10^{-2}$
Flare 1	17 ± 10
Low plateau	4 ± 3
High plateau 1	8 ± 4
Flare 2	17 ± 9
High plateau 2	8 ± 3
Flare 3	15 ± 7

(two high and one low) and three flares. The count rate of each interval is presented in Table 3. These intervals will be used for separate spectral analysis in the next section.

We searched for the NS spin pulse, with negative results. In Fig. 3, we present the resulting Lomb–Scargle periodogram. The expected frequencies of the pulse and subsequent harmonics have been marked. No significant signal is revealed.

We searched for a time delay between the Fe Kα line and the hard continuum. To this end, we produced the line (6.25–6.55 keV) and the hard continuum (7–12 keV) light curves, for the flare, plateau, and the whole light curve, respectively, and applied the cross-correlation method described in Ding et al. (2021). To obtain a reliable value of the time delay, the cross-correlation was calculated 5000 times with different random light-curve re-samplings. The result can be seen in Fig. 4. No relevant time delay was found. The obtained time delay was 40 ± 160 s for the flare section and 300 ± 600 s for the whole light curve, both compatible with 0.
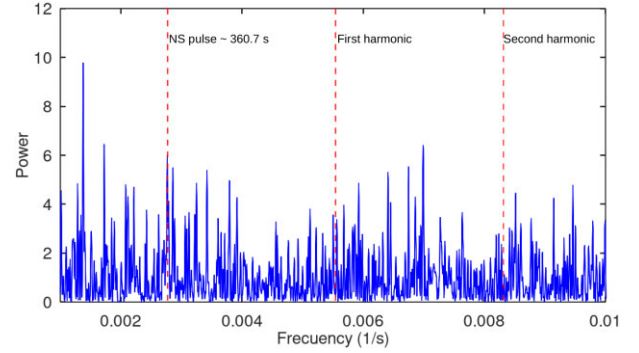

Figure 3. *Lomb–Scargle* periodogram for the three EPIC cameras combined light curve.
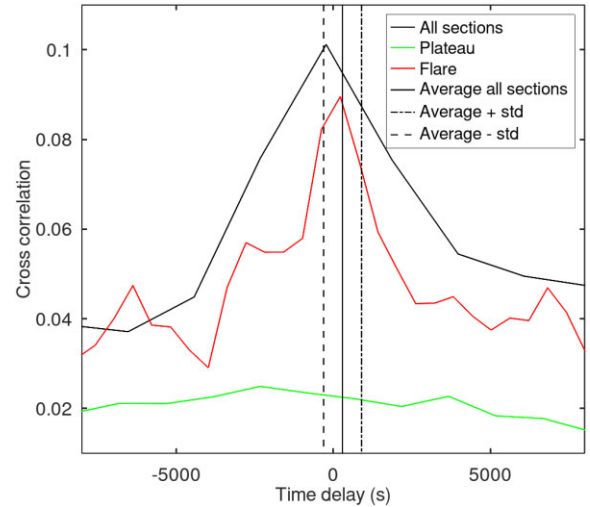

Figure 4. Example of one of the 5000 cross-correlation calculations performed to derive the time delay. A 150 s time bin was used in this particular case. The average time delay obtained for the whole light curve, from the 5000 iterations, plus/minus its standard deviation, are represented with vertical black lines.

3.2 Spectra: phenomenological model

We initially modelled the continuum using a blackbody plus a power law. This is the same model as used by Devasia & Paul (2018) for the analysis of the *Suzaku* data taken just before the X-ray eclipse (pre-eclipse, from now on). Besides the ISM absorption, we also allowed the presence of a local absorber, modulated by a partial covering fraction C, which acts as a proxy for the degree of clumping in the stellar wind of the donor star. The ISM absorption is modelled by the X-ray absorption model Tuebingen-Boulder `tbnew`. This model calculates the cross-section for X-ray absorption by the ISM as the sum of the cross-sections due to the gas phase, the grain phase, and the molecules in the ISM (Wilms, Allen & McCray 2000). For the *XMM–Newton* observation analysed here, the blackbody component was clearly negligible. The best fit was achieved by a simple photon power law where Γ is a dimensionless photon index and the normalization constant, K, is the spectral photons keV^{-1} cm^{-2} s^{-1} at 1 keV.

The model used is described as

$$F(E) = [\exp(-N_{H,1}\sigma(E)) + C \exp\left(-N_{H,2}\sigma(E)\right)] \left[K E^{-\Gamma} + G \right], \quad (1)$$
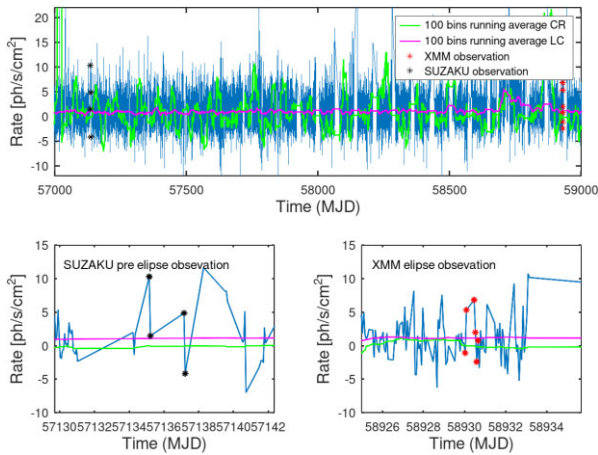
Figure 5. MAXI long-term light curve (upper panel) containing both observations. The lower panels show a zoom over the pre-eclipse (left-hand panel) and eclipse (right-hand panel) observations. Black and red asterisks correspond to the *Suzaku* and *XMM–Newton* observations, respectively. Magenta represents the 100 bin running average light-curve count rate and green represents the 100 bin running average CR.

where G represents the Gaussian functions added to account for the emission lines. Modelling the continuum during an eclipse is complicated because it is strongly suppressed and it is dominated by emission lines. To model the power law correctly, we have used the Monitor of All-sky X-ray Image (MAXI)[4] long-term light curve of the source (Matsuoka et al. 2009), plotted in Fig. 5, with both *Suzaku* and *XMM–Newton* observations marked. To help the analysis, we overplot the 100 bin running average for both the light curve and the colour ratio [CR = (4–10) keV/(2–4) keV]. No clear differences seem to exist between the two epochs. The source appears to be in the same long-term state. Besides the photoelectric absorption, X-ray photons are also scattered off the stellar wind. For the energies involved ($E < 10$ keV), the scattering is in the Thomson regime, with no energy dependence, that is to say, conserving the continuum spectral shape. When let to vary free, the photon index turns out to be $\Gamma = 0.5$, harder than during pre-eclipse. However, as stated before, the general state of the source appears to be essentially the same in both observations. Therefore, we fixed the power-law photon index to the pre-eclipse value ($\Gamma = 1.12$) in all our spectra. This worsened the average χ^2 fit by only 1.5 per cent. $N_{\mathrm{H.2}}$ ranged from 36 to 45, compatible with our model. The largest difference (~ 17 per cent) was $N_{\mathrm{H.1}}$, which ranged between 5.46 and 5.95. In any case, the obtained plasma parameters derived below are not sensitive to the photon index value and in general remain compatible within the uncertainties. The best-fitting parameters are presented in Tables 4 (continuum) and A1 (lines). The spectra are presented in Fig. 6.

Apart from the lack of the blackbody component, other differences arise when comparing with the pre-eclipse observation (Devasia & Paul 2018). Here, the covering fraction is $C \sim 1$ for all phases, while it was 0.68 during pre-eclipse.

The power-law norm was 100 times lower during the eclipse. For a given distance, the absorption-corrected fluxes of Table 4 translate into an X-ray luminosity ratio of ~ 70 between pre-eclipse and eclipse.[5] Such a ratio, although large, is well within the range found for eclipsing SGXBs (Aftab et al. 2019, their table 6).

In Table A1, we list the strongest lines found. The Fe line intensities respond positively to the continuum illumination. The intensity of the Fe Kα line, on the average spectrum, $I_{\mathrm{FeK\alpha}} = (10.4 \pm 0.9) \times 10^{-6}$ photons s^{-1} cm^{-2}, is ~ 7.4 times lower than the one measured during pre-eclipse, $I_{\mathrm{FeK\alpha}} = 77 \times 10^{-6}$ photons s^{-1} cm^{-2} (Devasia & Paul 2018). The presence of this emission from near-neutral Fe together with the highly ionized species, He-like Fe XXV and H-like Fe XXVI, means that the observed spectrum comes from gas in two phases, with very low and very high ionization, respectively. Fe XXVI/Fe XXV ratios are ~ 0.91, 0.59, 0.70, 0.66, and 0.33, for the average and flux resolved spectra, respectively. These values are compatible with a high ionization parameter $\log \xi \geq 3.4$ (Ebisawa et al. 1996, their table 5). However, Fe XXV/Si XIV ratios, namely 0.67, 0.40, 0.64, 0.46, and 1.88, are compatible with a plasma with an ionization parameter lower than 2.4 (Ebisawa et al. 1996).

3.3 Spectra: plasma emission code PHOTEMIS

Apart from the phenomenological model described in the preceding section, we have used a self-consistent plasma emission code. For that purpose, we use PHOTEMIS. This model describes the thermal (i.e. recombination and collisional excitation) emission, which comes from a plasma, using the XSTAR code (Kallman & Bautista 2001), without including the resonant scattered line emission. The model supplies the emissivity of the gas, in units of erg cm^{-3} s^{-1}. The model used was

$$F(E) = [\exp(-N_{\mathrm{H,1}}\sigma(E)) + C \exp\left(-N_{\mathrm{H,2}}\sigma(E)\right)] \times [\mathrm{photemis_1} + \mathrm{photemis_2} + \mathrm{powerlaw}], \quad (2)$$

where a power law is used to describe the continuum and PHOTEMIS the pure emission line spectrum. Two PHOTEMIS components, with low and high ionization parameters (ξ), respectively, are required to describe the main emission lines. The best-fitting parameters are presented in Table 5 and the corresponding data plus the fitted model in Fig. 7. As in the phenomenological model (see Section 3.2), the photon index value was set to the reported pre-eclipse value ($\Gamma = 1.12$).

The two plasmas have low ($\log \xi_1 \approx 0.36$) and high ($\log \xi_2 \approx 3.7$) ionization states. The fit requires broadening of the lines with a corresponding turbulence velocity of $v_{\mathrm{turb}} \approx 3000$ km s^{-1}. This velocity was maintaines during the fits to have the same value for both plasmas. The normalization of the cold plasma ($K_{\mathrm{phot_1}}$) is much larger than the one for the hot plasma ($K_{\mathrm{phot_2}}$). The physical meaning of the normalization (K_{phot}) is

$$K = \frac{\mathrm{EM}}{4\pi d^2} \times 10^{-10},$$

where $\mathrm{EM} = \int n_e n_i \mathrm{d}V \approx n^2 V$ is the emission measure of the gas (at the ionization parameter used in the fit) and d is the distance to the source. Therefore, the two gas phases have an emission measure ratio $\mathrm{EM_1/EM_2} = \mathrm{EM_{cold}/EM_{hot}} \approx 10^3$. For a source distance of $d \approx 7.4$ kpc, the $\mathrm{EM_{cold}} \approx 3 \times 10^{59}$ cm^{-3} and $\mathrm{EM_{hot}} \approx 2 \times 10^{56}$ cm^{-3}. These values are in agreement with those found for other SGXBs (i.e. Martínez-Chicharro et al. 2021).

4 DISCUSSION

The comparison of the eclipse and pre-eclipse spectra allows us to extract interesting conclusions. During eclipse, the observed spectrum is the sum of the scattered radiation plus the intrinsic X-ray

Table 4. Phenomenological model continuum (absorbed power law) spectral parameters (Fig. 6).

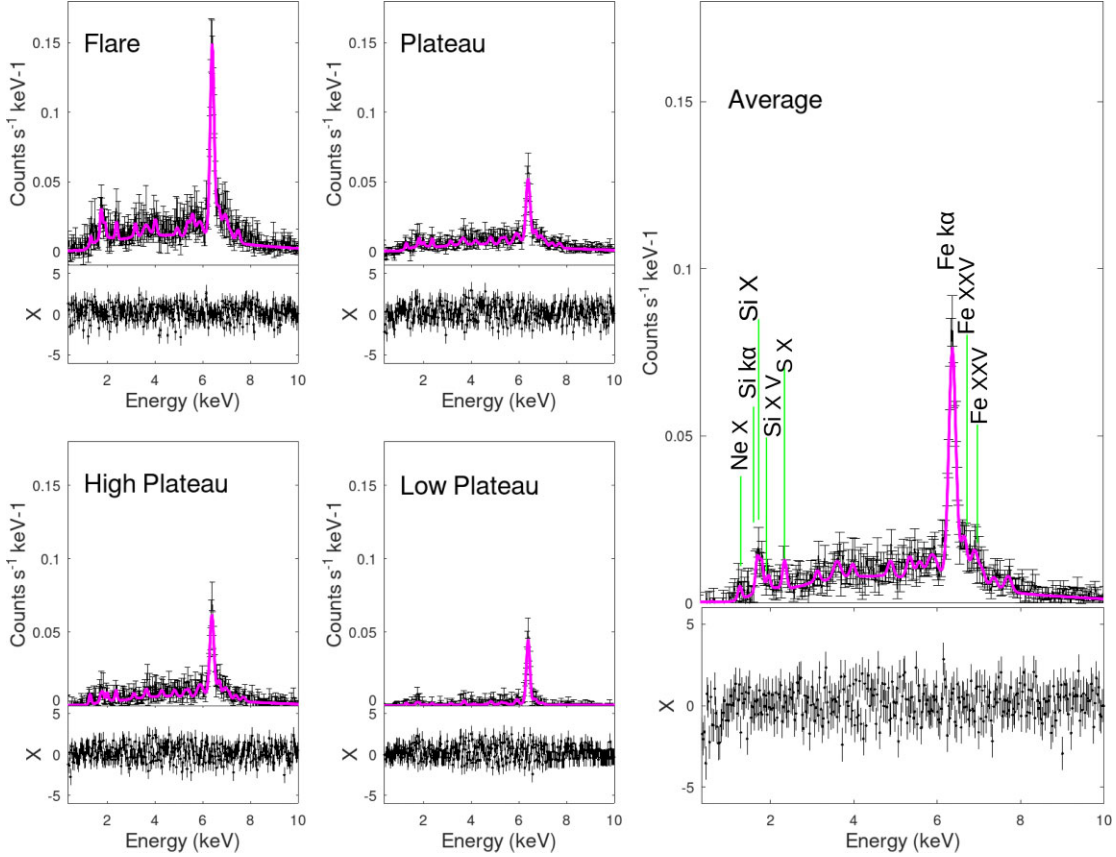|	Average	Flare	Plateau	High plateau	Low plateau
χ^2	1.32	1.19	1.21	1.09	0.99
$N_{H,1}$ ($\times 10^{22}$ cm^{-2})	6.9 ± 0.4	5.7 ± 0.4	$7.1^{+0.6}_{-0.4}$	$6.9^{+0.5}_{-0.4}$	$8.4^{+0.8}_{-0.6}$
C	$1.00^{+0.01}_{-0.12}$	$1.00^{+0.01}_{-0.10}$	$0.7^{+0.3}_{-0.2}$	$1.00^{+0.01}_{-0.17}$	$0.8^{+0.2}_{-0.6}$
$N_{H,2}$ ($\times 10^{22}$ cm^{-2})	39 ± 11	28^{+18}_{-14}	40^{+30}_{-20}	36^{+15}_{-13}	$\left(1.0^{+0.7}_{-1.0}\right) \times 10^2$
K_{po} ($\times 10^{-5}$ photons keV^{-1} cm^{-2} s^{-1})	3.4 ± 0.4	$4.8^{+0.9}_{-1.0}$	2.8 ± 0.4	2.8 ± 0.4	$0.41^{+0.10}_{-0.13}$
Flux ($\times 10^{-13}$ erg cm^{-2} s^{-1})	7.6 ± 0.9	13^{+3}_{-2}	5.6 ± 0.8	6.3 ± 0.9	$1.6^{+0.5}_{-0.4}$

Figure 6. Phenomenological model (power law plus Gaussians) fitted to the eclipse spectrum: data (black) and model (magenta) for the average and flux resolved spectra, respectively. All spectra are represented in the same scale to appreciate variability. Only the most relevant lines detected are marked in the average spectrum. The corresponding data are in Tables 4 (continuum) and A1 (lines).

Table 5. PHOTEMIS model spectral parameters (Fig. 7).

|	Average	Flare	Plateau	High plateau	Low plateau
χ^2	1.53	1.23	1.45	1.3	1.06
$N_{H,1}$	8.0 ± 0.4	$7.1^{+0.6}_{-0.3}$	$7.7^{+0.6}_{-0.5}$	$7.9^{+0.7}_{-0.6}$	11^{+2}_{-2}
C	$1.00^{+0.01}_{-0.05}$	$1.00^{+0.01}_{-0.08}$	$1.00^{+0.01}_{-0.07}$	$1.00^{+0.01}_{-0.07}$	$1.00^{+0.01}_{-0.15}$
$N_{H,2}$	44^{+6}_{-5}	51^{+9}_{-8}	40^{+7}_{-6}	41^{+7}_{-6}	28^{+12}_{-7}
K_{po}	4.2 ± 0.2	6.6 ± 0.4	3.1 ± 0.2	3.4 ± 0.2	$0.38^{+0.07}_{-0.07}$
K_{phot_1}	4000 ± 300	8000 ± 700	2700 ± 240	3300 ± 300	1900^{+120}_{-240}
$\log(\xi_1)$	$0.36^{+0.01}_{-0.08}$	$0.36^{+0.01}_{-0.08}$	$0.36^{+0.01}_{-0.08}$	$0.36^{+0.01}_{-0.08}$	$0.36^{+0.01}_{-0.08}$
K_{phot_2}	2.9 ± 0.5	$5.8^{+1.9}_{-1.0}$	2.0 ± 0.5	2.3 ± 0.6	$0.5^{+0.2}_{-0.3}$
$\log(\xi_2)$	3.30 ± 0.08	$3.40^{+0.07}_{-0.10}$	3.30 ± 0.07	3.30 ± 0.07	3.0 ± 0.2
v_{turb}	2400^{+600}_{-1000}	2100^{+900}_{-1800}	2800^{+200}_{-1300}	2600^{+400}_{-1400}	300^{+400}_{-10}
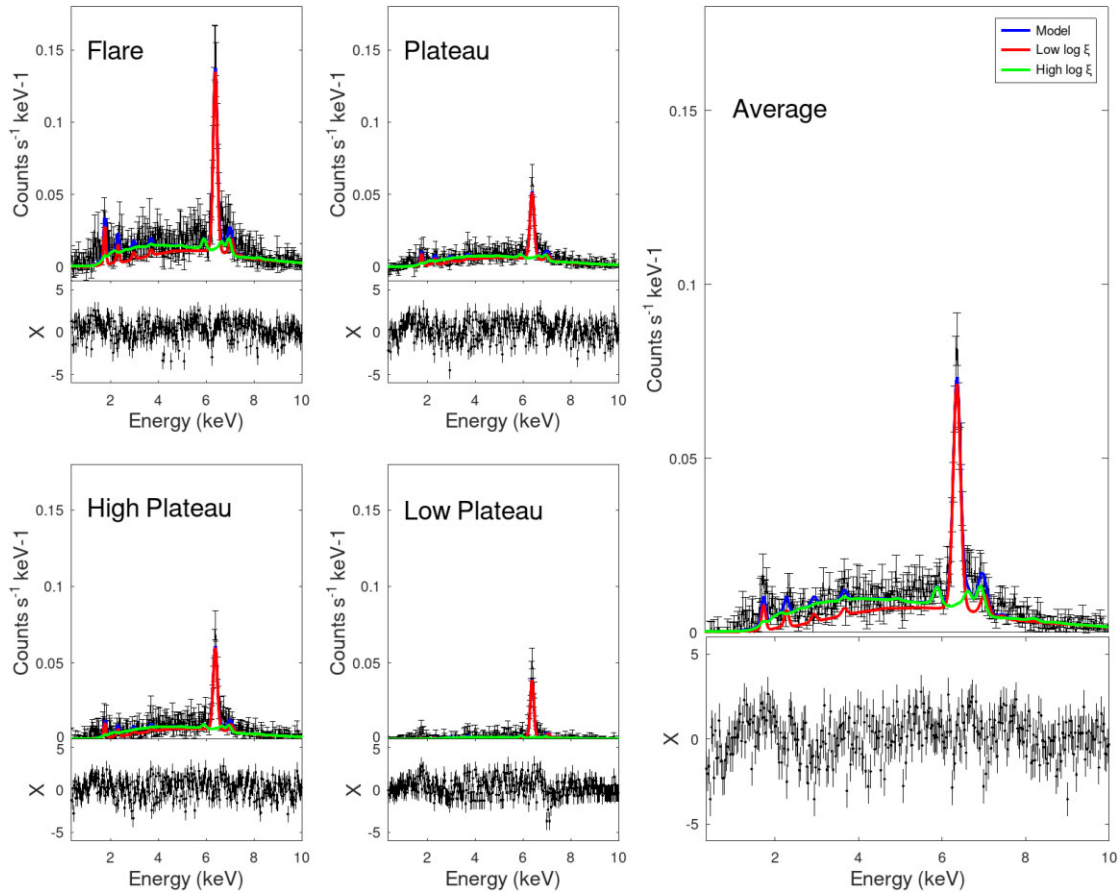
Figure 7. PHOTEMIS model of the eclipse spectra: blue is the model, red the low ionized component, and green the highly ionized component. The right-hand panel presents the average spectrum. In the left-hand column, from the top left-hand panel to the bottom right-hand panel, the flare, plateau, low plateau, and high plateau spectra are represented at the same scale to appreciate variations. The corresponding parameters are summarized in Table 5.

emission from the donor star. OB stars have X-ray luminosities of the order of 10^{32} erg s^{-1} (e.g. Nebot Gómez-Morán & Oskinova 2018), 100 times lower than observed here and, also, soft thermal spectra with $kT \sim 0.1–0.2$ keV. Therefore, the observed EPIC spectrum (0.35–10 keV) is clearly dominated by the scattered component. This is consistent with the time delay found, compatible with zero, as both observed components, Fe Kα line and hard continuum, are reflected (scattered) in the donor's wind, during eclipse.

The blackbody component of the pre-eclipse model, with a temperature of $kT_{bb} = 0.12$ keV, used to describe the soft excess at low energies, is not detected during eclipse. This rules out its origin as the stellar wind of the donor. It has to be produced close to the NS or at the accretion stream along the line connecting the NS and the donor.

The power-law photon index during eclipse is compatible with the pre-eclipse value. However, the absorption-corrected $L_X^{eclipse} \approx 1.5 \times 10^{34}$ erg s^{-1} is 70 times lower than pre-eclipse ($L_X \approx 1.0 \times 10^{36}$ erg s^{-1}). Such a ratio is rather large albeit well within those found in eclipsing SGXBs (Aftab et al. 2019, their table 6). To further explore this issue, we have compiled data from some eclipsing systems in Table C1. In this table, δ refers to the difference in path travelled by an X-ray photon emitted at orbital phase 0 and a photon emitted in the closest-to-observer phase. In order to calculate this distance, the semimajor axis, eccentricity, inclination, and argument of the periapsis were taken into account. In Fig. 8, we plot the wind density

integrated along this path versus the flux ratio (column density). Two conclusions can be extracted. First, there is a positive trend for all systems with class I–II donors (LMC X-4 is class III), indicating that absorption is a major driver of the observed flux ratio. Secondly, our source XTE J1855−026 is high on this trend but within the normal values displayed by eclipsing HMXBs. Deep X-ray eclipses, which allow for large out-of-eclipse to eclipse luminosity ratios, are possible provided that the wind occulted by the donor star (the X-ray shadow) is unionized, so that every scattered photon entering it is locally absorbed (Hertz, Joss & Rappaport 1978, their fig. 4, corresponding to model 2a).

The intensity of the Fe Kα line, on the average spectrum, $I_{FeK\alpha} = (10.4 \pm 0.9) \times 10^{-6}$ photons s^{-1} cm^{-2}, is ∼7.4 times lower than the one measured during pre-eclipse, $I_{FeK\alpha} = 77 \times 10^{-6}$ photons s^{-1} cm^{-2} (Devasia & Paul 2018). Fe Kα photons cannot be resonantly scattered in the wind because they do not have the required energy ($E_{Kedge} > 7.112$ keV) to induce further fluorescence. Therefore, these photons must be produced in the direct line of sight towards the observer and the NS, simultaneously. This means that the vast majority of Fe Kα emission must come from distances $r_X < 1R_*$ from the NS (Fig. 9).

As explained in Section 3.2, two plasmas, at different ionization states, are required to describe the eclipse spectrum. These two gas phases can be identified with the clumped part of the wind (cold and dense) and the interclump medium (hot and rarefied). The observed
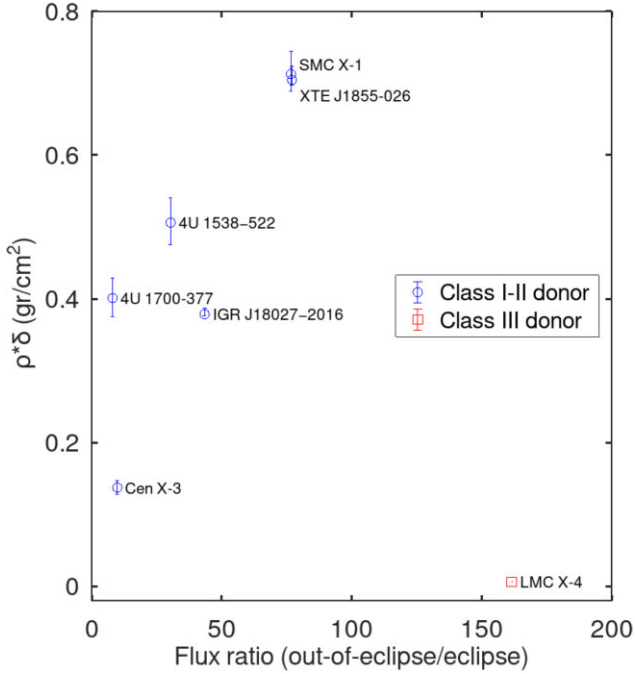
Figure 8. δ represents the difference in path travelled by a photon emitted at orbital phase 0 and a photon emitted in the closest-to-observer phase. This magnitude, multiplied by the wind density along this path, $\rho(r)$, is depicted versus the flux ratio between eclipse and out-of-eclipse observations within the 0.3–10.0 keV energy range.
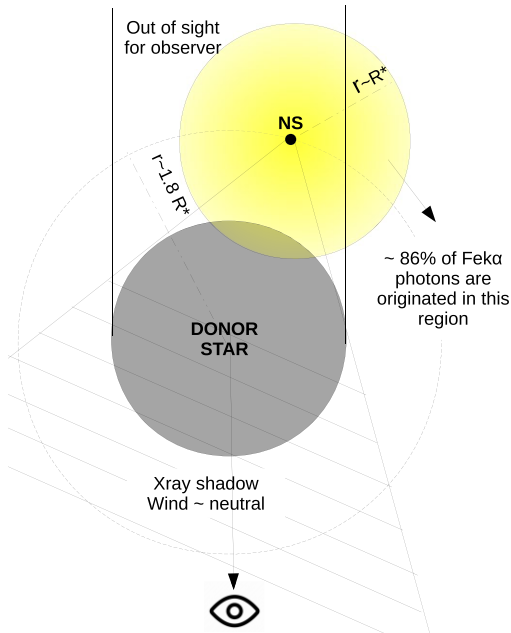

Figure 9. Scheme of the system. The orbit, donor star, and the Fe Kα emitting region are to scale.

ratio $EM_1/EM_2 = EM_{cold}/EM_{hot} \approx 10^3$ allows us to compute the density contrast n_c/n_i between the clump and interclump gas phases. Indeed,

$$EM_{cold}/EM_{hot} \approx \left(\frac{n_c}{n_i}\right)^2 \left(\frac{V_c}{V_i}\right), \tag{3}$$

where V_c and V_i are the wind volumes occupied by the clumps and the interclump medium, respectively, and $V_{wind} = V_c + V_i$. This can be expressed as a function of the clump volume filling factor, $f_V = V_{cl}/V_{wind}$, as

$$EM_{cold}/EM_{hot} = \left(\frac{n_c}{n_i}\right)^2 \frac{f_V}{1 - f_V}. \tag{4}$$

Now, assuming $f_V \approx 0.04$–0.05 (Sako et al. 1999; Martínez-Chicharro et al. 2021, for the cases of Vela X-1, B0.5I, $f_V \approx 0.04$ and QV Nor, O6.5I, $f_V \approx 0.05$, respectively), we get $n_c/n_i \approx 180$, in line with expectations from stellar wind models for massive stars (Oskinova et al. 2011; Hainich et al. 2020).

5 SUMMARY AND CONCLUSIONS

We present the first X-ray observation of the HMXB XTE J1855−026 taken entirely during the eclipse of the NS. This allows us to (a) compare with the parameters obtained during the existing pre-eclipse observation and (b) explore the back-illuminated stellar wind of the B0I donor. The main conclusions are:

(i) The blackbody component, used to describe the soft excess during pre-eclipse, is not observed during eclipse. It must be then produced near the NS or along the donor–NS line.

(ii) The 0.3–10 keV luminosity during eclipse ($\sim 10^{34}$ erg s^{-1}) is 70 times lower than pre-eclipse, well within the range found for eclipsing SGXBs. This large ratio would not be due to a different state of the source, as suggested by the long-term light curve, but due to deeper X-ray eclipses caused by the absorption of scattered photons in the non-illuminated part of the wind.

(iii) The intensity of the Fe Kα line, on the average eclipse spectrum, is ~ 7.4 times lower than the one measured during pre-eclipse. Since Kα photons cannot be resonantly scattered in the wind, the vast majority of Fe Kα emission must come from distances $r_X < 1R_*$ from the NS.

(iv) The eclipse spectrum is successfully modelled through the addition of two photoionized plasmas, one with low ionization (log $\xi_{1,cold} = 0.36$) and high emission measure ($EM_{1,cold} \approx 3 \times 10^{59}$ cm^{-3}) and another with high ionization (log $\xi_{2,hot} = 3.7$) and low emission measure ($EM_{2,hot} \approx 2 \times 10^{56}$ cm^{-3}).

(v) Assuming that the cold and hot gas phases are the clumps and the interclump medium of the stellar wind, respectively, and a clump volume filling factor $f_V \approx 0.04$–0.05, as observed for massive stars, a density contrast between clumps and the interclump medium of $n_c/n_i \approx 180$ is deduced in agreement with theoretical expectations and optical–ultraviolet observations of massive star winds.

ACKNOWLEDGEMENTS

DATA AVAILABILITY

The observation can be found in the *XMM–Newton* archive under the observation ID 0844630101.

REFERENCES

Abbott B. P. et al., 2016, Phys. Rev. Lett., 116, 061102

Aftab N., Paul B., Kretschmar P., 2019, ApJS, 243, 29

Augello G., Iaria R., Robba N. R., Salvo T. D., Burderi L., Lavagetto G., Stella L., 2003, ApJ, 596, L63

Bailer-Jones C. A. L., Rybizki J., Fouesneau M., Demleitner M., Andrae R., 2021, AJ, 161, 147

Bildsten L. et al., 1997, ApJS, 113, 367

Clark J. S., Goodwin S. P., Crowther P. A., Kaper L., Fairbairn M., Langer N., Brocksopp C., 2002, A&A, 392, 909

Coleiro A., Chaty S., 2013, ApJ, 764, 185

Corbet R. H. D., Mukai K., 2002, ApJ, 577, 923

Corbet R. H. D., Marshall F. E., Peele A. G., Takeshima T., 1999, ApJ, 517, 956

Devasia J., Paul B., 2018, J. Astrophys. Astron., 39, 7

Ding Y. Z. et al., 2021, MNRAS, 506, 2712

Ebisawa K., Day C. S. R., Kallman T. R., Nagase F., Kotani T., Kawashima K., Kitamoto S., Woo J. W., 1996, PASJ, 48, 425

Falanga M., Bozzo E., Lutovinov A., Bonnet-Bidaud J. M., Fetisova Y., Puls J., 2015, A&A, 577, A130

González-Galán A., 2016, preprint (arXiv:1503.01087)

Hainich R. et al., 2020, A&A, 634, A49

Hertz P., Joss P. C., Rappaport S., 1978, ApJ, 224, 614

Hill A. B. et al., 2005, A&A, 439, 255

Houck J. C., 2002, Annual Rev. Astron. & Astrophys., 41, 291

Islam N., Paul B., 2016, MNRAS, 461, 816

Jones C., Forman W., Tananbaum H., Schreier E., Gursky H., Kellogg E., Giacconi R., 1973, ApJ, 181, L43

Kallman T., Bautista M., 2001, ApJS, 133, 221

Kretschmar P. et al., 2019, New Astron. Rev., 86, 101546

Levine A., Rappaport S., Deeter J. E., Boynton P. E., Nagase F., 1993, ApJ, 410, 328

Levine A. M., Rappaport S. A., Zojcheski G., 2000, ApJ, 541, 194

Martínez-Chicharro M. et al., 2021, MNRAS, 501, 5646

Martínez-Núñez S. et al., 2017, Space Sci. Rev., 212, 59

Matsuoka M. et al., 2009, PASJ, 61, 999

Mukherjee U., Raichur H., Paul B., Naik S., Bhatt N., 2007, J. Astrophys. Astron., 27, 411

Nebot Gómez-Morán A., Oskinova L. M., 2018, A&A, 620, A89

Oskinova L. M., Todt H., Ignace R., Brown J. C., Cassinelli J. P., Hamann W.-R., 2011, MNRAS, 416, 1456

Parkes G. E., Murdin P. G., Mason K. O., 1978, MNRAS, 184, 73P

Penny A. J., Olowin R. P., Penfold J. E., Warren P. R., 1973, MNRAS, 163, 7P

Primini F., Rappaport S., Joss P. C., 1977, ApJ, 217, 543

Raichur H., Paul B., 2010, MNRAS, 401, 1532

Reynolds A. P., Bell S. A., Hilditch R. W., 1992, MNRAS, 256, 631

Reynolds A. P., Hilditch R. W., Bell S. A., Hill G., 1993, MNRAS, 261, 337

Sako M., Liedahl D. A., Kahn S. M., Paerels F., 1999, ApJ, 525, 921

Thompson A., 2009, X-ray Data Booklet. Lawrence Berkeley National Laboratory, University of California, Berkeley

Torrejón J. M., Negueruela I., Smith D. M., Harrison T. E., 2010, A&A, 510, A61

Torrejón J. M., Schulz N. S., Nowak M. A., Oskinova L., Rodes-Roca J. J., Shenar T., Wilms J., 2015, ApJ, 810, 102

Turner M. J. L. et al., 2001, A&A, 365, L27

van den Heuvel E. P. J., 2019, High-mass X-ray Binaries: Illuminating the Passage from Massive Binaries to Merging Compact Objects. Proc. IAUnion, Vol. 346. p. 1

van der Meer A., Kaper L., van Kerkwijk M. H., Heemskerk M. H. M., van den Heuvel E. P. J., 2007, A&A, 473, 523

Wilms J., Allen A., McCray R., 2000, ApJ, 542, 914

APPENDIX A: STRONG EMISSION LINES

Table A1. Parameters of the strongest lines found in the average and flux resolved spectra (Fig. 6; ATOMDB data base).

		Average	Flare	Plateau	High plateau	Low plateau
Ne X	I ($\times 10^{-6}$ photons s^{-1} cm^{-2})	110^{+120}_{-80}	90^{+60}_{-50}	370^{+300}_{-200}	340^{+300}_{-200}	270^{+240}_{-190}
	Centre (keV)	1.32 ± 0.07	$1.40^{+0.04}_{-0.03}$	$1.30^{+0.03}_{-0.04}$	$1.30^{+0.05}_{-0.04}$	$1.30^{+0.02}_{-0.06}$
	Sigma (eV)	20^{+1}_{-20}	20^{+1}_{-20}	20^{+1}_{-20}	20^{+1}_{-20}	1^{+20}_{-0}
	Eqw (eV)	4000^{+4000}_{-2000}	2600^{+1600}_{-1500}	6000^{+4000}_{-3000}	14000^{+12000}_{-8000}	7000^{+6000}_{-5000}
Si Kα	I ($\times 10^{-6}$ photons s^{-1} cm^{-2})	10^{+0}_{-3}	10^{+0}_{-4}	10^{+0}_{-4}	10^{+0}_{-4}	8^{+2}_{-4}
	Centre (keV)	$1.72^{+0.02}_{-0.01}$	1.72 ± 0.01	1.72 ± 0.01	1.72 ± 0.01	1.72 ± 0.01
	Sigma (eV)	1^{+20}_{-0}	2^{+20}_{-0}	1^{+20}_{-1}	1^{+20}_{-1}	1^{+20}_{-1}
	Eqw (eV)	550^{+0}_{-160}	380^{+0}_{-160}	660^{+0}_{-240}	700^{+0}_{-300}	3900^{+700}_{-2000}
Si XIII/Fe XXIV	I ($\times 10^{-6}$ photons s^{-1} cm^{-2})	7 ± 3	8^{+2}_{-6}	6^{+3}_{-3}	5^{+4}_{-3}	2^{+2}_{-2}
	Centre (keV)	$1.83^{+0.01}_{-0.02}$	$1.81^{+0.02}_{-0.01}$	$1.83^{+0.01}_{-0.02}$	$1.82^{+0.01}_{-0.03}$	$1.83^{+0.01}_{-0.02}$
	Sigma (eV)	4^{+20}_{-3}	20^{+1}_{-20}	$2^{+20.0}_{-1}$	1^{+20}_{-0}	2^{+20}_{-1}
	Eqw (eV)	420 ± 170	320^{+80}_{-240}	440^{+220}_{-210}	370^{+280}_{-240}	1100^{+1200}_{-1000}
Si XIII	I ($\times 10^{-6}$ photons s^{-1} cm^{-2})	3^{+2}_{-2}	7^{+4}_{-4}	3 ± 2	4^{+2}_{-2}	$0.4^{+0.9}_{-0.4}$
	Centre (keV)	$1.99^{+0.04}_{-0.05}$	$1.93^{+0.04}_{-0.03}$	$2.00^{+0.04}_{-0.04}$	$2,00^{+0.04}_{-0.04}$	$2.05^{+0.06}_{-0.15}$
	Sigma (eV)	1^{+20}_{-0}	10^{+10}_{-9}	1^{+20}_{-0}	1^{+20}_{-0}	1^{+20}_{-0}
	Eqw (eV)	180^{+130}_{-110}	310 ± 10	200 ± 130	280^{+170}_{-160}	200^{+400}_{-200}
S XII	I ($\times 10^{-6}$ photons s^{-1} cm^{-2})	4^{+1}_{-1}	5^{+3}_{-2}	3 ± 1	3 ± 2	0.8 ± 0.7
	Centre (keV)	$2.38^{+0.02}_{-0.02}$	$2.39^{+0.02}_{-0.04}$	$2.37^{+0.03}_{-0.03}$	$2.38^{+0.03}_{-0.03}$	$2.37^{+0.04}_{-0.08}$
	Sigma (eV)	1^{+20}_{-0}	20^{+1}_{-20}	1^{+20}_{-0}	1^{+20}_{-0}	1^{+20}_{-0}
	Eqw (eV)	290^{+110}_{-100}	290^{+140}_{-130}	260 ± 130	280 ± 140	500 ± 500
Fe Kα	I ($\times 10^{-6}$ photons s^{-1} cm^{-2})	10^{+1}_{-1}	20^{+2}_{-6}	8 ± 1	9 ± 1	8 ± 1
	Centre (keV)	6.41 ± 0.01	$6.41^{+0.01}_{-0.02}$	6.40 ± 0.01	6.40 ± 0.01	6.40 ± 0.01
	Sigma (eV)	40^{+14}_{-18}	40^{+20}_{-40}	50^{+17}_{-21}	50^{+20}_{-24}	1^{+30}_{-0}
	Eqw (eV)	2500^{+180}_{-200}	3200^{+300}_{-900}	2500 ± 240	2500 ± 300	15300^{+1500}_{-1400}
Fe XXV	I ($\times 10^{-6}$ photons s^{-1} cm^{-2})	2^{+1}_{-1}	3^{+2}_{-2}	2^{+1}_{-1}	2 ± 1	$1.0^{+0.3}_{-0.4}$
	Centre (keV)	$6.69^{+0.03}_{-0.04}$	$6.67^{+0.05}_{-0.08}$	6.70 ± 0.04	$6.70^{+0.04}_{-0.05}$	6.70 ± 0.04
	Sigma (eV)	1^{+100}_{-1}	1^{+100}_{-0}	1^{+100}_{-0}	1^{+100}_{-0}	$1.0^{+70.0}_{-0.1}$
	Eqw (eV)	500^{+300}_{-200}	500 ± 300	470^{+210}_{-220}	500 ± 240	1600^{+600}_{-800}
Fe XXVI	I ($\times 10^{-6}$ photons s^{-1} cm^{-2})	2^{+1}_{-1}	2^{+2}_{-2}	1^{+1}_{-1}	1^{+1}_{-1}	$0.3^{+0.4}_{-0.3}$
	Centre (keV)	6.93 ± 0.06	$6.85^{+0.15}_{-0.01}$	6.93 ± 0.07	$6.95^{+0.05}_{-0.10}$	$6.96^{+0.04}_{-0.11}$
	Sigma (eV)	30^{+70}_{-30}	2^{+100}_{-1}	1^{+100}_{-0}	1^{+100}_{-0}	1^{+100}_{-0}
	Eqw (eV)	400^{+300}_{-200}	300 ± 300	400^{+50}_{-200}	350^{+180}_{-240}	700^{+1000}_{-700}

APPENDIX B: EMISSION LINES

Best-fitting parameters for all the Gaussians included in the phenomenological model (see Section 3.2).

Table B1. Tentative identification and parameters of weaker lines found in the average and flux resolved spectra.

		Average	Flare	Plateau	High plateau	Low plateau
Ar XVII	I ($\times 10^{-6}$ phtons s^{-1} cm^{-2})	0.5 ± 0.5	1 ± 1	$0.3^{+0.5}_{-0.3}$	$0.4^{+0.6}_{-0.4}$	$0.1^{+0.3}_{-0.1}$
	Centre (keV)	$3.17^{+0.23}_{-0.07}$	$3.19^{+0.21}_{-0.07}$	$3.15^{+0.24}_{-0.05}$	$3.13^{+0.24}_{-0.03}$	$3.17^{+0.23}_{-0.07}$
	Sigma (eV)	1^{+20}_{-0}	1^{+20}_{-0}	1^{+20}_{-0}	1^{+20}_{-0}	1^{+20}_{-0}
	Eqw (eV)	50 ± 50	90 ± 80	30^{+60}_{-30}	50^{+80}_{-50}	120^{+240}_{-120}
Ca Kα	I ($\times 10^{-6}$ photons s^{-1} cm^{-2})	$0.8^{+0.6}_{-0.5}$	$0.9^{+1.0}_{-0.8}$	$0.6^{+0.6}_{-0.4}$	$0.7^{+0.5}_{-0.5}$	0.4 ± 0.3
	Centre (keV)	$3.64^{+0.05}_{-0.06}$	$3.63^{+0.17}_{-0.13}$	$3.67^{+0.06}_{-0.09}$	$3.66^{+0.05}_{-0.07}$	$3.71^{+0.04}_{-0.04}$
	Sigma (eV)	30^{+70}_{-30}	1^{+100}_{-0}	1^{+100}_{-0}	1^{+100}_{-0}	$1.0^{+80.0}_{-0.1}$
	Eqw (eV)	110^{+70}_{-60}	80^{+120}_{-70}	100^{+90}_{-70}	110 ± 80	500 ± 300
Ca XIX	I ($\times 10^{-6}$ photons s^{-1} cm^{-2})	$0.4^{+0.4}_{-0.3}$	$0.9^{+0.8}_{-0.7}$	$0.1^{+0.3}_{-0.1}$	0.4 ± 0.4	$0.01^{+0.20}_{-0.01}$
	Centre (keV)	$4.01^{+0.09}_{-0.12}$	$4.02^{+0.06}_{-0.12}$	$4.2^{+0.1}_{-0.3}$	$4.3^{+0.1}_{-0.4}$	$4.0^{+0.3}_{-0.1}$
	Sigma (eV)	1^{+20}_{-0}	10^{+10}_{-9}	1^{+20}_{-0}	20^{+0}_{-20}	16^{+4}_{-15}
	Eqw (eV)	50 ± 50	90^{+80}_{-70}	20^{+40}_{-20}	3 ± 3	3 ± 3
Cr Kα/Ca XX	I ($\times 10^{-6}$ photons s^{-1} cm^{-2})	0.7 ± 0.3	$0.8^{+1.3}_{-0.8}$	0.4 ± 0.4	0.6 ± 0.4	0.2 ± 0.2
	Centre (keV)	$5.4^{+0.1}_{-0.1}$	$5.4^{+0.4}_{-0.2}$	$5.3^{+0.5}_{-0.3}$	$5.38^{+0.06}_{-0.12}$	$5.3^{+0.5}_{-0.3}$
	Sigma (eV)	20^{+1}_{-20}	1^{+20}_{-0}	1^{+20}_{-0}	20^{+1}_{-20}	1^{+20}_{-0}
	Eqw (eV)	130 ± 60	120^{+180}_{-110}	140^{+150}_{-140}	140 ± 90	400 ± 400
Cr Kβ/Mn Kα	I ($\times 10^{-6}$ photons s^{-1} cm^{-2})	$1.1^{+0.8}_{-0.3}$	$1.9^{+0.9}_{-1.2}$	1.5 ± 0.5	$1.1^{+0.8}_{-0.4}$	0.6 ± 0.2
	Centre (keV)	$5.94^{+0.05}_{-0.08}$	$5.88^{+0.12}_{-0.12}$	$5.93^{+0.04}_{-0.04}$	$5.95^{+0.05}_{-0.06}$	$5.93^{+0.03}_{-0.03}$
	Sigma (eV)	2^{+100}_{-1}	100^{+1}_{-100}	80^{+30}_{-70}	1^{+100}_{-0}	1^{+70}_{-0}
	Eqw (eV)	310^{+220}_{-90}	290^{+130}_{-190}	370^{+120}_{-120}	400^{+300}_{-100}	1100 ± 400
Fe XXVI	I ($\times 10^{-6}$ photons s^{-1} cm^{-2})	$0.9^{+0.6}_{-0.9}$	3^{+1}_{-2}	$0.8^{+0.6}_{-0.8}$	$0.8^{+0.5}_{-0.8}$	$0.1^{+0.4}_{-0.1}$
	Centre (keV)	$7.12^{+0.08}_{-0.07}$	$7.00^{+0.19}_{-0.01}$	$7.10^{+0.09}_{-0.08}$	$7.11^{+0.09}_{-0.08}$	$7.06^{+0.14}_{-0.06}$
	Sigma (eV)	1^{+20}_{-0}	1^{+20}_{-0}	1^{+20}_{-0}	1^{+20}_{-0}	1^{+20}_{-0}
	Eqw (eV)	230^{+150}_{-230}	400^{+200}_{-300}	230^{+170}_{-230}	240^{+160}_{-240}	100^{+400}_{-100}
Ni Kα	I ($\times 10^{-6}$ photons s^{-1} cm^{-2})	0.9 ± 0.4	$1.4^{+0.9}_{-1.2}$	0.9 ± 0.4	0.9 ± 0.5	$0.03^{+0.20}_{-0.03}$
	Centre (keV)	$7.4^{+0.1}_{-0.1}$	$7.21^{+0.19}_{-0.01}$	$7.40^{+0.01}_{-0.02}$	$7.40^{+0.01}_{-0.02}$	$7.40^{+0.01}_{-0.20}$
	Sigma (eV)	1^{+20}_{-0}	1^{+20}_{-0}	1^{+20}_{-0}	1^{+20}_{-0}	1^{+20}_{-0}
	Eqw (eV)	250 ± 110	260^{+180}_{-230}	270^{+20}_{-10}	300 ± 160	70^{+400}_{-70}
Co Kβ/Ni XXVI	I ($\times 10^{-6}$ photons s^{-1} cm^{-2})	1.2 ± 0.4	2.2 ± 0.9	1.0 ± 0.5	0.8 ± 0.5	0.1 ± 0.1
	Centre (keV)	7.7 ± 0.1	7.5 ± 0.1	7.7 ± 0.1	7.7 ± 0.1	$7.7^{+0.1}_{-0.2}$
	Sigma (eV)	20^{+1}_{-20}	20^{+1}_{-20}	1^{+20}_{-0}	1^{+20}_{-0}	1^{+20}_{-0}
	Eqw (eV)	360 ± 120	440^{+180}_{-170}	350 ± 160	280 ± 160	400^{+600}_{-400}

APPENDIX C: ECLIPSING SYSTEM PARAMETERS

Table C1. Eclipsing systems.

Source	Donor spectral type	Companion radius ($R_\odot$)	Inclination i (°)	Semimajor axis a ($R_\odot$)	Eccentricity e	ω (°)	v_∞ (km s^{-1})	$\dot{M}$ ($\times 10^7$ M$_\odot$ yr^{-1})	Ratio (°)	δ ($R_\odot$)
Cen X-3	O6,5 II–III (1)	12.1 ± 0.5 (1)	65 ± 1 (6)	18.84 ± 0.02 (11)	≤0.0016 (16)	0 ± 0(6)	2050 ± 600 (6)	5.3(6)	9.79 (19)	16 ± 1
LMC X-4	O8 III (1)	7.8 ± 0.4 (1)	59.3 ± 9 (6)	13.19 ± 0.04 (12)	0.0006 ± 0.0002 (12)	0 ± 0(6)	1950 ± 600(6)	2.4 (6)	237.18* (19)	13 ± 3
SMC X-1	B0 I (2)	18 ± (7)	62 ± 2 (6)	26.08 ± 0 (13)	≤0.0007 (7)	166 ± 12(6)	870 ± 260(6)	15(6)	76.62 (19)	24 ± 1
4U 1700−377	O7f (3)	21.9 ± 1.3 (8)	62 ± 1 (6)	31.69 ± 4.2(14)	≤0.0008 (17)	49 ± 11 (6)	1850 ± 550(6)	21(6)	8.01 (19)	30 ± 1
4U 15382−22	B0Iab (4)	17.2 ± 1 (9)	67 ± 1 (6)	24.84 ± 37 (15)	0.174 ± 0.015(15)	40 ± 12(6)	1000 ± 300 (6)	8.3 (6)	30.28 (19)	19 ± 1
IGR J180272−2016	B1-Ib (5)	19.2 ± 4.2 (10)	72 ± 2 (6)	30.78 ± 0 (10)	0.2 ± 0 (18)	0 ± 0(6)	680 ± 200(6)	6.3 (6)	43.38 (19)	19 ± 2
XTE J1855−026	B0Iaep (6)	22 ± 2 (6)	71 ± 2 (6)	36.65 ± 17.27 (6)	0.04 ± 2 (6)	226 ± 15 (6)	620 ± 190(6)	65 (6)	∼ 70	24 ± 2

Note. References: (1) van der Meer et al. (2007), (2) Reynolds et al. (1993), (3) Penny et al. (1973), (4) Parkes, Murdin & Mason (1978), (5) Torrejón et al. (2010), (6) Falanga et al. (2015), (7) Primini, Rappaport & Joss (1977), (8) Clark et al. (2002), (9) Reynolds, Bell & Hilditch (1992), (10) Hill et al. (2005), (11) Raichur & Paul (2010), (12) Levine, Rappaport & Zojcheski (2000), (13) Levine et al. (1993), (14) Jones et al. (1973), (15) Mukherjee et al. (2007), (16) Bildsten et al. (1997), (17) Islam & Paul (2016), (18) Augello et al. (2003), and (19) Aftab et al. (2019).
*Mean value.

This paper has been typeset from a T$_{\rm E}$X/L$^{\rm A}$T$_{\rm E}$X file prepared by the author.